44th AIAA Aerospace Sciences Meeting and Exhibit
9-12 January 2006, Reno, Nevada

AIAA 2006-1448

Submitted to the 44th AIAA Aerospace Sciences Meeting and Exhibit, January 9–12, 2006, Reno, Nevada, U.S.A.

Parallel Adaptive Mesh Refinement Scheme for Turbulent Non-Premixed Combusting Flow Prediction

X. Gao* and C. P. T. Groth†

University of Toronto Institute for Aerospace Studies
4925 Dufferin Street, Toronto, Ontario, M3H 5T6, Canada

A parallel adaptive mesh refinement (AMR) algorithm is proposed for predicting turbulent non-premixed combusting flows characteristic of gas turbine engine combustors. The Favre-averaged Navier-Stokes equations governing mixture and species transport for a reactive mixture of thermally perfect gases in two dimensions, the two transport equations of the k-ω turbulence model, and the time-averaged species transport equations, are all solved using a fully coupled finite-volume formulation. A flexible block-based hierarchical data structure is used to maintain the connectivity of the solution blocks in the multi-block mesh and facilitate automatic solution-directed mesh adaptation according to physics-based refinement criteria. This AMR approach allows for anisotropic mesh refinement and the block-based data structure readily permits efficient and scalable implementations of the algorithm on multi-processor architectures. Numerical results for turbulent non-premixed diffusion flames, including cold- and hot-flow predictions for a bluff body burner, are described and compared to available experimental data. The numerical results demonstrate the validity and potential of the parallel AMR approach for predicting complex non-premixed turbulent combusting flows.

I. Introduction

In the last twenty years, numerical methods have become an essential tool for the investigation of turbulent combusting flows. Due to more manageable computational requirements and somewhat greater ease in handling complex flow geometries, most practical simulation algorithms are based on the Reynolds- or Favre-averaged Navier-Stokes equations, where the turbulent flow structure is entirely modelled and not resolved. In spite of simplifications offered by the time-averaging approach, the system of equations governing turbulent combusting flows can be both large and stiff and its solution can still place severe demands on available computational resources.

Many approaches have been taken to reduce the computational costs of simulating combusting flows. One successful approach is to make use of solution-directed mesh adaptation, such as the adaptive mesh refinement refinement (AMR) algorithms developed for aerospace applications.[1–11] Computational grids that automatically adapt to the solution of the governing equations are very effective in treating problems with disparate length scales, providing the required spatial resolution while minimizing memory and storage requirements. Recent progress in the development and application of AMR algorithms for low-Mach-number reacting flows and premixed turbulent combustion is described by Day and Bell.[12–14] Another approach for coping with the computational cost of reacting flow prediction is to apply a domain decomposition procedure

*PhD Candidate, Email: gao@utias.utoronto.ca, Student Member AIAA
†Associate Professor, Email: groth@utias.utoronto.ca, Senior Member AIAA

and solve the problem in a parallel fashion using multiple processors. Large massively parallel distributed-memory computers can provide many fold increases in processing power and memory resources beyond those of conventional single-processor computers and would therefore provide an obvious avenue for greatly reducing the time required to obtain numerical solutions of combusting flows. Douglas *et al.*[15] describe a parallel algorithm for numerical combustion modelling. More recently, Northrup and Groth[16] combined these two numerical approaches, producing a parallel AMR method that both reduces the overall problem size and the time to calculate a solution for laminar combusting flows. The extension of this combined approach to turbulent non-premixed combusting flows is the focus of the present study.

II. Mathematical Model of Turbulent Combusting Flows

A. Favre-Averaged Navier-Stokes Equations

A mathematical model based on the Favre-averaged Navier-Stokes equations for a compressible thermally perfect reactive mixture of gases has been formulated and is used herein to describe turbulent non-premixed combustion processes. In this formulation, the continuity, momentum, and energy equations for the reactive mixture of N species are

$$\frac{\partial \rho}{\partial t} + \boldsymbol{\nabla} \cdot (\rho \vec{\mathbf{u}}) = 0 \,, \tag{1}$$

$$\frac{\partial}{\partial t}(\rho \vec{\mathbf{u}}) + \boldsymbol{\nabla} \cdot \left(\rho \vec{\mathbf{u}} \vec{\mathbf{u}} + p \vec{\vec{\mathbf{I}}} \right) = \boldsymbol{\nabla} \cdot \left(\vec{\vec{\boldsymbol{\tau}}} + \vec{\vec{\boldsymbol{\lambda}}} \right) + \vec{\mathbf{f}} \,, \tag{2}$$

$$\frac{\partial}{\partial t}(\rho e) + \boldsymbol{\nabla} \cdot \left[\rho \vec{\mathbf{u}} \left(e + \frac{p}{\rho} \right) \right] = \boldsymbol{\nabla} \cdot \left[\left(\vec{\vec{\boldsymbol{\tau}}} + \vec{\vec{\boldsymbol{\lambda}}} \right) \cdot \vec{\mathbf{u}} \right] + \boldsymbol{\nabla} \cdot (D_k \boldsymbol{\nabla} k) - \boldsymbol{\nabla} \cdot (\vec{\mathbf{q}} + \vec{\mathbf{q}}_t) + \vec{\mathbf{u}} \cdot \vec{\mathbf{f}} \,, \tag{3}$$

where ρ is the time-averaged mixture density, $\vec{\mathbf{u}}$ is the Favre-averaged mean velocity of the mixture, p is the time-averaged mixture pressure, $e = |\vec{\mathbf{u}}|^2/2 + \sum_{n=1}^{N} c_n h_n - p/\rho + k$ is the Favre-averaged total specific mixture energy, $\vec{\mathbf{f}}$ is a body force per unit volume acting on the gaseous mixture, k is the specific turbulent kinetic energy, D_k is the coefficient for the diffusion of the turbulent energy, $\vec{\vec{\boldsymbol{\tau}}}$ and $\vec{\vec{\boldsymbol{\lambda}}}$ are the molecular and turbulent Reynolds stress tensors or diads, and $\vec{\mathbf{q}}$ and $\vec{\mathbf{q}}_t$ are the molecular and turbulent heat flux vectors, respectively. The mixture pressure is given by the ideal gas law

$$p = \sum_{n=1}^{N} \rho c_n R_n T \,, \tag{4}$$

where R_n is the species gas constant and T is the mixture temperature. Fourier's law is used to represent the thermal diffusion caused by the random thermal motion and turbulence. In addition, h_n is the absolute (chemical and sensible) internal enthalpy for species n. The transport equation describing the time evolution of the species mass fraction, c_n, is given by

$$\frac{\partial}{\partial t}(\rho c_n) + \boldsymbol{\nabla} \cdot (\rho c_n \vec{\mathbf{u}}) = -\boldsymbol{\nabla} \cdot \left(\vec{\boldsymbol{\mathcal{J}}}_n + \vec{\boldsymbol{\mathcal{J}}}_{tn} \right) + \rho \dot{w}_n \,, \tag{5}$$

where $\dot{w}_n$ is the time-averaged or mean rate of the change of the species mass fraction produced by the chemical reactions and $\vec{\boldsymbol{\mathcal{J}}}_n$ and $\vec{\boldsymbol{\mathcal{J}}}_{tn}$ are the molecular and turbulent diffusive fluxes for species n, respectively. The latter are specified using Fick's law. The modified two-equation k-ω model of Wilcox[17] is used here to model the unresolved turbulent flow quantities. In this approach, the Boussinesq approximation is used to relate the Reynolds stress tensor, $\vec{\vec{\boldsymbol{\lambda}}}$, to the mean flow strain-rate tensor using a turbulent eddy viscosity, μ_t,

$$\lambda_{ij} = \mu_t \left[\frac{\partial u_i}{\partial x_j} + \frac{\partial u_j}{\partial x_i} - \frac{2}{3} \delta_{ij} \frac{\partial u_k}{\partial x_k} \right] - \frac{2}{3} \delta_{ij} \rho k \,, \tag{6}$$

with $\mu_t = \rho k/\omega$. Transport equations are solved for turbulent kinetic energy, k, and the specific dissipation rate, ω, given by

$$\frac{\partial}{\partial t}(\rho k) + \boldsymbol{\nabla}\cdot(\rho k\vec{\mathbf{u}}) = \vec{\vec{\boldsymbol{\lambda}}} : \boldsymbol{\nabla}\vec{\mathbf{u}} + \boldsymbol{\nabla}\cdot[(\mu + \mu_t\sigma^*)\,\boldsymbol{\nabla}k] - \beta^*\rho k\omega\,, \tag{7}$$

$$\frac{\partial}{\partial t}(\rho\omega) + \boldsymbol{\nabla}\cdot(\rho\omega\vec{\mathbf{u}}) = \alpha\frac{\omega}{k}\vec{\vec{\boldsymbol{\lambda}}} : \boldsymbol{\nabla}\vec{\mathbf{u}} + \boldsymbol{\nabla}\cdot[(\mu + \mu_t\sigma)\,\boldsymbol{\nabla}\omega] - \beta\rho\omega^2\,, \tag{8}$$

where μ is the molecular viscosity of the mixture and σ^*, β^*, α, σ, and β are closure coefficients for the two-equation model. The latter are given by

$$\alpha = \frac{13}{25}\,, \quad \beta = \beta_\circ f_\beta\,, \quad \beta^* = \beta^*_\circ f_{\beta^*}\,, \quad \sigma = \sigma^* = \frac{1}{2}\,, \tag{9}$$

with

$$\beta_\circ = \frac{9}{125}\,, \quad \beta^*_\circ = \frac{9}{100}\,, \tag{10}$$

$$f_\beta = \frac{1+70\chi_\omega}{1+80\chi_\omega}\,, \quad f_{\beta^*} = \begin{cases} 1 & \chi_k \le 0\,, \\ \dfrac{1+680\chi_k^2}{1+400\chi_k^2} & \chi_k > 0\,, \end{cases}\,, \tag{11}$$

and

$$\chi_\omega = \left|\frac{\Omega_{ij}\Omega_{jk}S_{ki}}{(\beta^*_\circ\omega)^3}\right|\,, \quad \chi_k = \frac{1}{\omega^3}\frac{\partial k}{\partial x_j}\frac{\partial\omega}{\partial x_j}\,. \tag{12}$$

The tensors Ω_{ij} and S_{ik} are the vorticity and strain rate tensors, respectively.

For two-dimensional axisymmetric flows, the preceding equations can be re-expressed using vector notation as

$$\frac{\partial\mathbf{U}}{\partial t} + \frac{\partial}{\partial r}(\mathbf{F} - \mathbf{F}_v) + \frac{\partial}{\partial z}(\mathbf{G} - \mathbf{G}_v) = \frac{1}{r}\left(\mathbf{S}_\phi + \mathbf{S}_{\phi_v}\right) + \mathbf{S} \tag{13}$$

where $\mathbf{U}$ is the vector of conserved variables given by

$$\mathbf{U} = \left[\ \rho,\, \rho v_r,\, \rho v_z,\, \rho e,\, \rho k,\, \rho\omega,\, \rho c_1,\, \ldots,\, \rho c_N\ \right]^{\mathrm{T}}\,, \tag{14}$$

the inviscid and viscous radial flux vectors, $\mathbf{F}$ and $\mathbf{F}_v$, are

$$\mathbf{F} = \begin{bmatrix} \rho v_r \\ \rho v_r^2 + p \\ \rho v_r v_z \\ (\rho e + p)v_r \\ \rho k v_r \\ \rho\omega v_r \\ \rho v_r c_1 \\ \vdots \\ \rho v_r c_N \end{bmatrix}\,, \quad \mathbf{F}_v = \begin{bmatrix} 0 \\ \tau_{rr} + \lambda_{rr} \\ \tau_{rz} + \lambda_{rz} \\ v_r(\tau_{rr} + \lambda_{rr}) + v_z(\tau_{rz} + \lambda_{rz}) - q_r - q_{t_r} + (\mu + \mu_t\sigma^*)\frac{\partial k}{\partial r} \\ (\mu + \mu_t\sigma^*)\frac{\partial k}{\partial r} \\ (\mu + \mu_t\sigma)\frac{\partial\omega}{\partial r} \\ -\mathcal{J}_{1r} - \mathcal{J}_{t1r} \\ \vdots \\ -\mathcal{J}_{Nr} - \mathcal{J}_{tNr} \end{bmatrix}\,, \tag{15}$$

the inviscid and viscous axial flux vectors, $\mathbf{G}$ and $\mathbf{G}_v$, are

$$\mathbf{G} = \begin{bmatrix} \rho v_z \\ \rho v_r v_z \\ \rho v_z^2 + p \\ (\rho e + p) v_z \\ \rho k v_z \\ \rho \omega v_z \\ \rho v_z c_1 \\ \vdots \\ \rho v_z c_N \end{bmatrix}, \quad \mathbf{G}_v = \begin{bmatrix} 0 \\ \tau_{zr} + \lambda_{zr} \\ \tau_{zz} + \lambda_{zz} \\ v_r(\tau_{zr} + \lambda_{zr}) + v_z(\tau_{zz} + \lambda_{zz}) - q_z - q_{t_z} + (\mu + \mu_t \sigma^*)\frac{\partial k}{\partial z} \\ (\mu + \mu_T \sigma^*)\frac{\partial k}{\partial z} \\ (\mu + \mu_T \sigma)\frac{\partial \omega}{\partial z} \\ -\mathcal{J}_{1z} - \mathcal{J}_{t1z} \\ \vdots \\ -\mathcal{J}_{Nz} - \mathcal{J}_{tNz} \end{bmatrix}, \tag{16}$$

and $\mathbf{S}_\phi$ and $\mathbf{S}_{\phi_v}$ are the inviscid and viscous source vectors associated with the axisymmetric geometry, and $\mathbf{S}$ is the source vector containing terms related to the finite rate chemistry, body force due to gravity, and turbulence modelling, respectively. The latter have the form

$$\mathbf{S}_\phi = \begin{bmatrix} -\rho v_r \\ -\rho v_r^2 \\ -\rho v_r (\rho e + p) \\ -\rho k v_r \\ -\rho \omega v_r \\ -\rho c_1 v_r \\ \vdots \\ -\rho c_N v_r \end{bmatrix}, \quad \mathbf{S}_{\phi_v} = \begin{bmatrix} 0 \\ (\tau_{rr} + \lambda_{rr}) - (\tau_{\theta\theta} + \lambda_{\theta\theta}) \\ \tau_{rz} + \lambda_{rz} \\ \mathcal{W} - q_r - q_{t_r} + (\mu + \mu_t \sigma^*)\frac{\partial k}{\partial r} \\ (\mu + \mu_t \sigma^*)\frac{\partial k}{\partial r} \\ (\mu + \mu_t \sigma)\frac{\partial \omega}{\partial r} \\ \mathcal{J}_{1r} + \mathcal{J}_{t1r} \\ \vdots \\ \mathcal{J}_{Nr} + \mathcal{J}_{tNr} \end{bmatrix}, \quad \mathbf{S} = \begin{bmatrix} 0 \\ 0 \\ \rho g_z \\ \rho v_z g_z \\ \mathcal{P} - \beta^* \rho k \omega \\ \alpha \frac{\omega}{k} \mathcal{P} - \beta \rho \omega^2 \\ \rho \dot{\omega_1} \\ \vdots \\ \rho \dot{\omega_N} \end{bmatrix}, \tag{17}$$

with

$$\mathcal{W} = v_r(\tau_{rr} + \lambda_{rr}) + v_z(\tau_{rz} + \lambda_{rz}), \tag{18}$$

$$\mathcal{P} = \lambda_{rr}\frac{\partial v_r}{\partial r} + \lambda_{rz}\left(\frac{\partial v_r}{\partial z} + \frac{\partial v_z}{\partial r}\right) + \lambda_{zz}\frac{\partial v_z}{\partial z} + \lambda_{\theta\theta}\frac{v_r}{r}. \tag{19}$$

Here, r, z, and θ are the radial, axial, and azimuthal coordinates of the axisymmetric frame, v_r and v_z are the radial and axial velocity components, g_z is the acceleration due to gravity (assumed to have only an axial component here), q_r and q_z the radial and axial components of the heat flux, τ_{rr}, τ_{rz}, τ_{zz}, and $\tau_{\theta\theta}$ are the components of the viscous fluid stresses, and λ_{rr}, λ_{rz}, λ_{zz}, and $\lambda_{\theta\theta}$ are the Reynolds stresses.

B. Thermodynamic and Transport Properties

Thermodynamic relationships and transport coefficients are required to close the system of equations given above. Thermodynamic and molecular transport properties of each gaseous species are prescribed using the empirical database compiled by Gordon and McBride,[18,19] which provides curve fits for the species enthalpy, h_n, specific heat, c_{p_n}, entropy, viscosity, μ_n, and thermal conductivity, κ_n, as functions of temperature, T. For example, the enthalpy and viscosity for a particular species is given by

$$h_n = R_n T\left[-a_{1,n}T^{-2} + a_{2,n}T^{-1}\ln T + a_{3,n} + \frac{a_{4,n}}{2}T + \frac{a_{5,n}}{3}T^2 + \frac{a_{6,n}}{4}T^3 + \frac{a_{7,n}}{5}T^4 + b_1 T^{-1}\right] + \Delta h^o_{f_n}, \tag{20}$$

$$\ln \mu_n = A_n \ln T + \frac{B_n}{T} + \frac{C_n}{T^2} + D_n, \tag{21}$$

where $a_{k,n}$, A_n, B_n, C_n, and D_n are the coefficients for the curve fits. The Gordon-McBride dataset contains curve fits for over 2000 substances, including 50 reference elements.

The molecular viscosity, μ, and thermal conductivity, κ, of the reactive mixture are determined using the mixture rules of Wilke[20] and Mason and Saxena,[21] respectively. Turbulent contributions to thermal conductivity and species diffusivity are modelled by making an analogy between momentum and heat transfer and introducing the turbulent Prandtl and Schmidt numbers, Pr_t and Sc_t, both of which are taken to be constant ($\mathrm{Pr}_t = 0.9$ and $\mathrm{Sc}_t = 1$), and assuming $\kappa_t = \mu_t c_p / \mathrm{Pr}_t$ and $D_{t_n} = \mu_t / \rho \mathrm{Sc}_t$.

C. Reduced Chemical Kinetics and Eddy Dissipation Model

For methane-air combustion considered in the present work, the following reduced, one-step, five-species, chemical kinetic scheme of Westbrook and Dryer[22] is used:

$$\mathrm{CH_4} + 2\ \mathrm{O_2} \rightarrow \mathrm{CO_2} + 2\ \mathrm{H_2O}\,. \tag{22}$$

The five species are methane (CH_4), oxygen (O_2), carbon dioxide (CO_2), water (H_2O), and nitrogen (N_2). Nitrogen is taken to be inert.

In order to account for the strong interaction that exists between the chemistry and turbulence in non-premixed combustion processes, the mean reaction rate, $\dot{w}_n$, is estimated using the eddy dissipation model (EDM) of Magnussen and Hjertager.[23] This model assumes that turbulence mixing limits the fuel burning and the fuel reaction rate is limited by the deficient species. The individual species mean reaction rate is then taken to be the minimum of the rates given by the finite-rate chemical kinetics (i.e., the law of mass action and Arrhenius reaction rates) and the EDM value. The latter is related to the turbulence mixing time and is estimated using the dissipation rate, ω.

D. Treatment of Near-Wall Turbulence

Both low-Reynolds-number and wall-function formulations of the k-ω model are used for the treatment of near-wall turbulent flows, with a procedure for automatically switching from one to the other, depending on mesh resolution. In the case of the low-Reynolds-number formulation, it can be shown that

$$\lim_{y \to 0} \omega = \frac{6\nu}{\beta y^2}\,, \tag{23}$$

where y is the distance normal from the wall.[17] Rather than attempting to solve the ω-equation directly, the preceding expression is used to specify ω for all values of $y^+ \leq 2.5$, where $y^+ = u_\tau y/\nu$, $u_\tau^2 = \tau_w/\rho$, and τ_w is the wall shear stress. Provided there are 3-5 computational cells inside $y^+ = 2.5$, this procedure reduces numerical stiffness, guarantees numerical accuracy, and permits the k-ω model to be solved directly in the near-wall region without resorting to wall functions. In the case of the wall-function formulation, the expressions

$$\frac{u}{u_\tau} = \frac{1}{\kappa} \ln(y^+) + C\,, \tag{24}$$

$$k = \frac{u_\tau^2}{\sqrt{\beta^*}}\,, \tag{25}$$

$$\omega = \frac{u_\tau}{\sqrt{\beta^*}\kappa y}\,, \tag{26}$$

are used to fully specify k and ω for $y^+ \leq$ 30-250, where κ is the von Kármán constant. A procedure has been developed to automatically switch between these two approaches, depending on the near-wall mesh resolution. This automatic near-wall treatment readily accommodates situations during adaptive mesh refinement where the mesh resolution may not be sufficient for directly calculating near-wall turbulence using the low-Reynolds-number formulation.

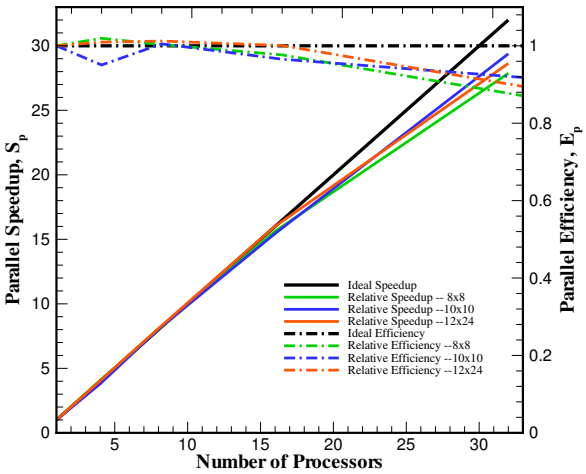

Figure 1. Relative parallel speed-up, S_p, and efficiency, E_p, for a fixed-size problem using up to 32 processors.

III. Parallel AMR Algorithm

A. Finite Volume Scheme

A finite volume scheme is employed to solve the Favre-averaged Navier-Stokes equations of Eq. 13 above for a two-dimensional axisymmetric coordinate frame. The system of governing equations is integrated over quadrilateral cells of a structured multi-block quadrilateral mesh. The semi-discrete form of this finite-volume formulation applied to cell (i, j) is given by

$$\frac{d\mathbf{U}_{i,j}}{dt} = -\frac{1}{A_{i,j}} \sum_{\text{faces},k} \vec{\mathbf{F}}_{i,j,k} \cdot \vec{\mathbf{n}}_{i,j,k} \Delta\ell_{i,j,k} + \frac{1}{r_{i,j}} \left(\mathbf{S}_{\phi_{i,j}} + \mathbf{S}_{\phi_{v_{i,j}}} \right) + \mathbf{S}_{i,j} \,, \tag{27}$$

where $\vec{\mathbf{F}} = (\mathbf{F} - \mathbf{F}_v, \mathbf{G} - \mathbf{G}_v)$ $r_{i,j}$ and $A_{i,j}$ are the radius and area of cell (i, j), and $\Delta\ell$ and $\vec{\mathbf{n}}$ are the length of the cell face and unit vector normal to the cell face or edge, respectively. The inviscid (hyperbolic) components of the numerical flux at each cell face is evaluated using limited linear reconstruction[24] and one of several Riemann-solver based flux functions.[25–27] The viscous (elliptic) components of the cell face flux are evaluated by employing a centrally-weighted diamond-path reconstruction procedure as described by Coirier and Powell.[28]

For the time-invariant calculations performed as part of this study, a preconditioned multigrid algorithm with multi-stage time marching scheme smoother is used to solve the coupled set of non-linear ordinary differential equations that arise from the finite-volume spatial discretization procedure. The smoother is based on the optimally-smoothing multi-stage time marching schemes developed by van Leer *et al.*[29] To cope with numerical stiffness, a semi-implicit treatment is used in the temporal discretization of the source terms associated with axisymmetric geometry, finite-rate chemistry, turbulence modelling, and gravitational acceleration. A nonlinear V-cycle multigrid approach is used in which the turbulence quantities are restricted to the coarse mesh but not updated so as to enhance the stability of the scheme and avoid non-physical solutions.[30, 31]

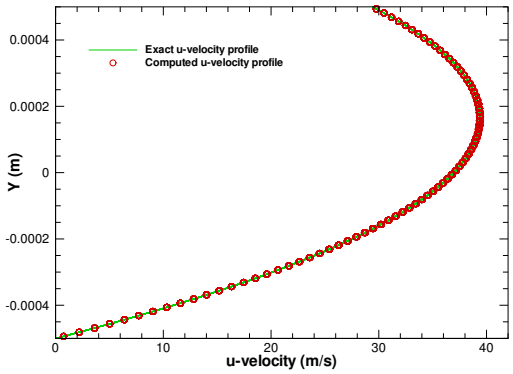

Figure 2. Comparison of predicted and exact solutions of the velocity profile for laminar Couette flow.

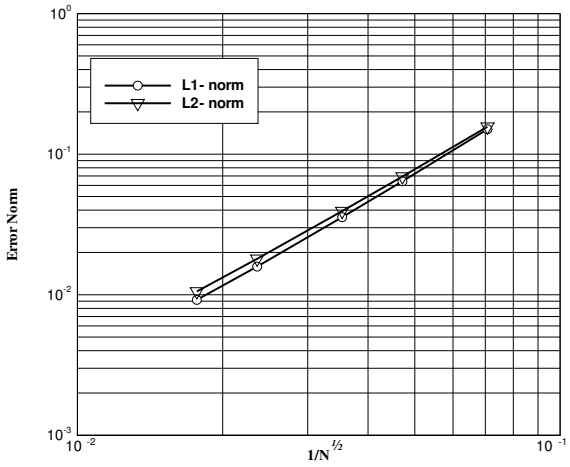

Figure 3. L_1- and L_2-norms of the solution error for laminar Couette flow.

B. Block-Based Adaptive Mesh Refinement

Adaptive mesh refinement algorithms, which automatically adapt the mesh to the solution of the governing equations, can be very effective in treating problems with disparate length scales. They permit local mesh refinement and thereby minimize the number of computational cells required for a particular calculation. Following the approach developed by Groth *et al.*[9,10] for computational magnetohydrodynamics, a flexible block-based hierarchical data structure has been developed and is used in conjunction with the finite-volume scheme described above to facilitate automatic solution-directed mesh adaptation on multi-block body-fitted quadrilateral mesh according to physics-based refinement criteria. The method allows for anisotropic mesh refinement and is well suited to parallel implementation via domain decomposition.

The AMR procedure is illustrated in Fig. 7, where a sequence of adaptively refined grids leading to a final mesh consisting of 235 12×8 cell blocks and 22,560 cells with five levels of refinement is shown. Refer to the recent papers by Sachdev *et al.*[11] and Northrup and Groth[16] for further details.

C. Domain Decomposition and Parallel Implementation

A parallel implementation of the block-based AMR scheme has been developed using the C++ programming language and the MPI (message passing interface) library.[32] A domain decomposition procedure is used where the solution blocks making up the computational mesh are distributed equally among available processors, with more than one block permitted per processor. A Morton ordering space filling curve is used to order the blocks for more efficient load balancing.[33]

The parallel implementation has been carried out on a parallel cluster of 4-way Hewlett-Packard ES40, ES45, and Integrity rx4640 servers with a total of 244 Alpha and Itanium 2 processors. A low-latency Myrinet network and switch is used to interconnect the servers in the cluster. Estimates of the parallel performance and scalability of the proposed solution-adaptive method on this facility are shown in Fig. 1 for a fixed-size turbulent non-reacting multi-species flow problem having 64 solution blocks. The relative parallel speed-up, S_p, defined as

$$S_p = \frac{t_1}{t_p} p \,, \tag{28}$$

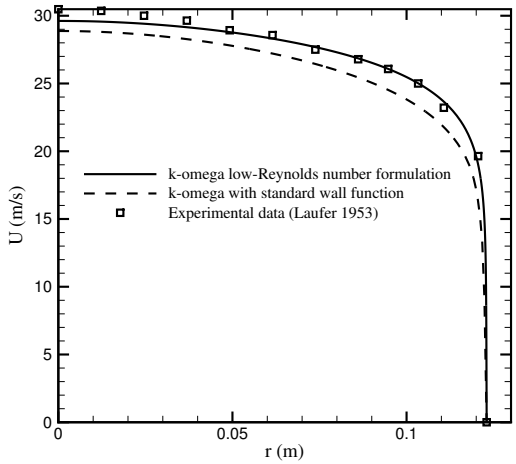

Figure 4. Comparison of predicted mean axial velocity with experimental data for fully developed pipe flow.

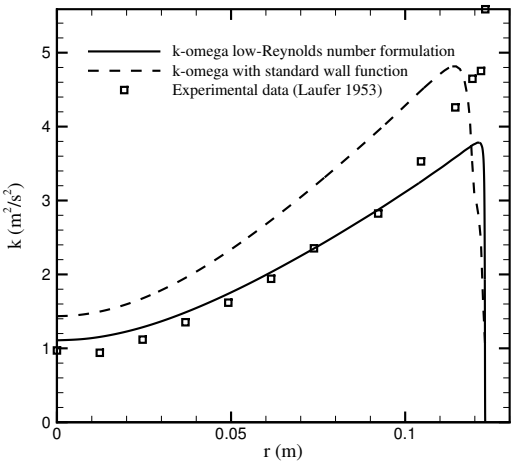

Figure 5. Comparison of predicted turbulent kinetic energy with experimental data for fully developed pipe flow.

and the relative parallel efficiency, E_p, defined as

$$E_p = \frac{S_p}{p}\,, \tag{29}$$

are both shown in the figure, where t_1 is the processor time required to solve the problem using a single processor, and t_p is the total processor time required to solve the problem using p processors. The performance indicators are shown for three different mesh sizes: 4,096 cells (64 8×8 cell blocks); 6,400 cells (64 10×10 cell blocks); and 18,432 cells (64 12×24 cell blocks). It can be seen that the parallel speed-up of block-based AMR scheme is nearly linear and is about 87% for up to 32 processors, even for the smaller 8×8 cell solution blocks. The parallel efficiency is 92% for the larger 10×10 cell solution blocks.

IV. Numerical Verification and Validation

A. Non-Reacting Laminar Couette Flow

The validation and verification of the proposed parallel AMR scheme has been carried out for laminar flows.[16] The computation of non-reacting laminar Couette flow in a channel with a moving wall was considered in order to demonstrate the accuracy of the viscous spatial discretization scheme. The case with an upper wall velocity of 29.4 m/s and a favourable pressure gradient of $dp/dx = -3,177$ Pa/m was investigated and compared to the analytic solution. The predicted velocity profile is plotted and compared to the exact analytic solution for this incompressible isothermal flow in Figure 2. The L_1- and L_2-norms of the error in axial component of velocity are plotted in Fig. 3. The slopes of the two norms are 2.02 and 1.95, respectively, indicating that the finite-volume scheme is indeed second-order accurate. The proposed scheme has also been found to provide predictions of axisymmetric co-flow methane-air diffusion flames that are in good agreement with experimental data.[16]

B. Non-Reacting Fully-Developed Turbulent Pipe Flow

The validation of the parallel AMR scheme for non-reacting turbulent flows has also been considered by comparing numerical results to the experimental data of Laufer[34] for non-reacting, fully-developed turbulent

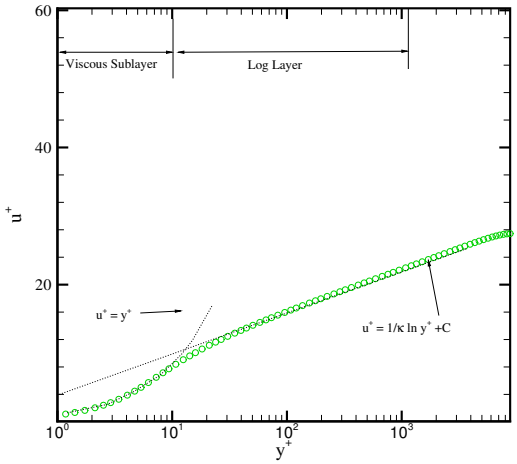

Figure 6. Predicted mean axial velocity profile in the near-wall region of fully developed pipe flow, Re = 500, 000.

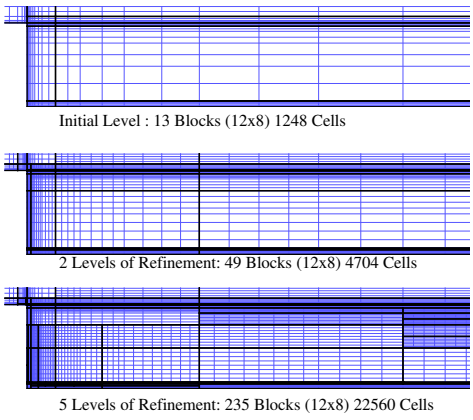

Figure 7. Sequence of adaptively refined mesh. The initial mesh consisted of 13 12×8 cell blocks and 1,248 cells and the final mesh consisted of 235, 12×8 cell blocks and 22,560 cells after five levels of refinement.

flow in a pipe with Re = 500, 000. Solutions for both the wall function and low-Reynolds-number formulations of the k-ω turbulence model are compared to measured mean axial velocity and turbulent kinetic energy profiles in Figs. 4–6. Calculations with the low-Reynolds-number formulation were performed using 80 cells in the radial direction with 3-4 of those cells lying within the laminar sublayer. The first cell off the wall was located at $y^+ \approx 0.6$. The results using the wall functions was obtained using 32 cells in the radial direction with the first cell located at $y^+ \approx 43$. The agreement between the experimental data and numerical results for this case is generally quite good. As expected, it is evident that the k-ω model is able to reproduce the characteristic features of fully-developed pipe flow and, in particular, the predictions using the low-Reynolds-number model are in excellent agreement with well-established theoretical results in the near-wall region.

V. Numerical Results for Bluff-Body Burner

A. Non-Reacting Flow

The International Workshops on Measurement and Computation of Turbulent Non-Premixed Flames have lead to the establishment of an internet library of well-documented turbulent non-premixed flames that are appropriate for combustion model validation.[35] Following the initial validation efforts described above, the proposed parallel AMR method was applied to the solution of two non-reacting flow cases associated with the bluff-body burner configuration that forms part of this experimental database. These bluff-body jet flows have been investigated and/or used for validation purposes in several recent studies (e.g., Dally *et al.*[36] and Turpin and Troyes[37]). For the cases considered, the diameter of the bluff body is $D_b = 50$ mm and the velocity and temperature of the co-flowing air is 20 m/s and 300 K, respectively. In the first case of interest, air is injected through an orifice of diameter 3.6 mm at the base of the cylindrical bluff body with a temperature of 300 K and velocity of 61 m/s. The Reynolds and Mach numbers based on the high-speed jet are Re = 193, 000 and Ma = 0.18. In the second case, ethylene (C_2H_4) is injected at the base of the bluff body with a velocity of 50 m/s and a temperature of 300 K. In this case, the Reynolds and Mach numbers based on the ethylene flow are Re = 145, 000 and Ma = 0.11.

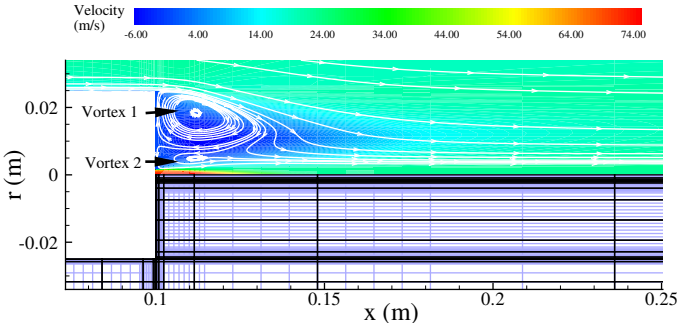

Figure 8. Predicted flow velocity and streamlines for non-reacting flow field of bluff-body burner.

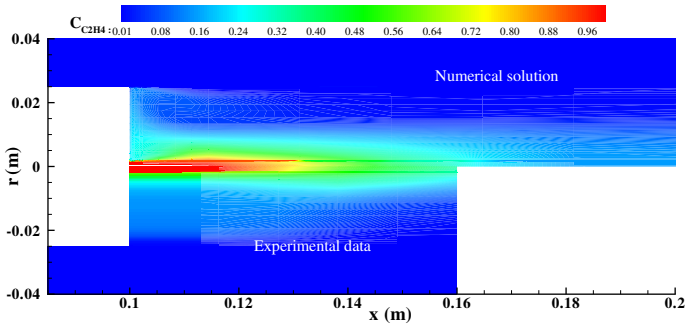

Figure 9. Predicted mean C_2H_4 mass fraction for non-reacting flow field of bluff-body burner.

Figure 8 shows the predicted mean velocity and streamlines for the air jet obtained using a mesh consisting of 320 6×6 cell blocks and 11,520 cells with five levels of refinement. Numerical results for the ethylene fuel jet are depicted in Fig. 9, where the predicted mass fraction of C_2H_4 obtained using a mesh consisting of 479 6×6 cell blocks and 17,244 cells, also with five levels of refinement, is compared to measured C_2H_4 concentrations. In both cases, the mesh resolution was such that the typical size of the computational cells nearest the wall was in the range $0.2 < y^+ < 1$.

For the air jet case, the overall flow field predictions are generally in good agreement with the experimental data (not shown) and reveal the formation of a double-vortex structure in the re-circulation zone which are important in controlling fuel/oxidizer mixing. The calculations indicate that the re-circulation zone extends to $x/D_b \approx 0.8$, where D_b is the bluff body diameter. This is slightly less than the experimentally observed value of $x/D_b \approx 1.0$. The agreement between the predictions and experiment is further confirmed by a comparison of the predicted radial profiles of the mean axial velocity component at both $x/D_b = 0.6$ and $x/D_b = 1.0$ downstream from the base of the bluff body to the measured data as shown in Figs. 10 and 11, and by a comparison of the predicted axial (centre-line) profile of the mean axial velocity component to experimental results as depicted in Fig. 12. For each profile, rather good agreement between the numerical predictions and experiment can be observed.

For the ethylene jet case, the predictions of the mixing field (Fig. 9) also appear to be quite reasonable when compared to the experimental data. Detailed comparisons of the predicted on-axis axial and radial distributions ($x/D_b = 0.6$ and $x/D_b = 1.0$) of the C_2H_4 mass fraction to measured values given in Figs. 13–15 also indicate that the fuel and oxidizer mixing process is quite well reproduced.

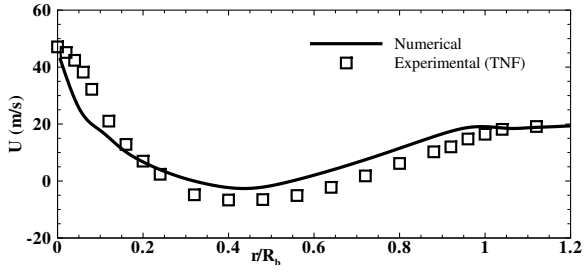

Figure 10. Comparison of predicted and measured radial profiles of the mean axial velocity component at $x/D_b = 0.6$ downstream from the base of the bluff body for non-reacting bluff-body burner with air jet.

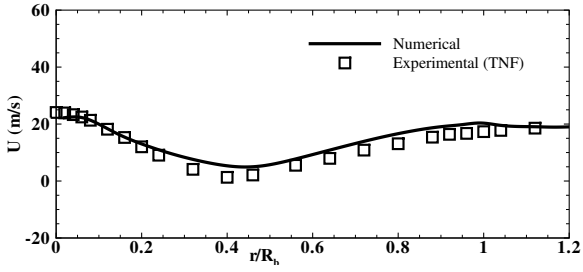

Figure 11. Comparison of predicted and measured radial profiles of the mean axial velocity component at $x/D_b = 1.0$ downstream from the base of the bluff body for non-reacting bluff-body burner with air jet.

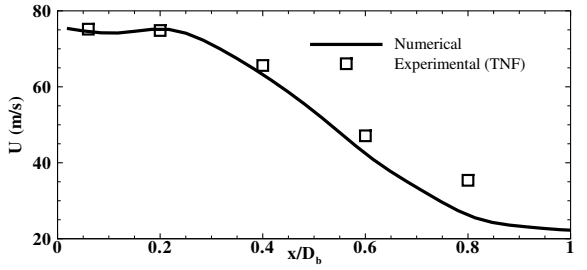

Figure 12. Comparison of predicted and measured on-axis axial profiles of the mean axial velocity component downstream from the base of the bluff body for non-reacting bluff-body burner with air jet.

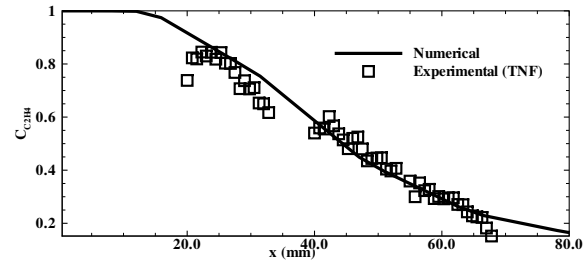

Figure 13. Comparison of predicted and measured on-axis axial profiles of the C_2H_4 mass fraction downstream from the base of the bluff body for non-reacting bluff-body burner with ethylene jet.

B. Reacting Flow

The numerical solution of a methane-air combusting flow field for the bluff-body burner described above has also been considered here. The flow geometry and boundary conditions for this reacting case are the same as those for the non-reacting cases, except that the velocities of the co-flowing air and methane fuel are 25 m/s and 108 m/s, respectively. The Reynolds and Mach numbers are Re = 315, 000 and Ma = 0.24. Computations were carried out using a mesh consisting of 91 8×8 cell blocks and 5,824 cells with four levels of refinement. As in the non-reacting cases, the mesh resolution was such that the typical size of the computational cells nearest the wall was in the range $0.2 < y^+ < 1$.

Figures 16 and 17 show the predicted distributions of mean temperature and mean mass fraction of CO_2 for this turbulent non-premixed flame. The predicted flame structure is generally in agreement with the experimentally observed structure. The flame is quite elongated and three zones can be identified: the re-circulation, neck, and jet-like propagation zones. A double-vortex structure is formed in the re-circulation zone and acts to stabilize the flame. The maximum flame temperature is about 2180 K. The predicted radial profiles of the mean temperature and mass fraction of CO_2 at $x/D_b = 1.92$ are also shown in Figs. 18 and 19 and are compared to several measured values of the flame temperature and carbon dioxide concentration. In general, the temperature and hence carbon dioxide concentration are somewhat overpredicted; however, the agreement with the experimental values is surprisingly good considering the limitations of the simplified reduced chemical kinetics scheme and turbulence/chemistry interaction model used herein.

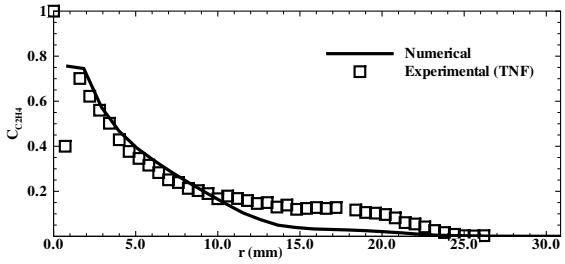

Figure 14. Comparison of predicted and measured radial profiles of the C_2H_4 mass fraction at $x/D_b = 0.6$ downstream from the base of the bluff body for non-reacting bluff-body burner with ethylene jet.

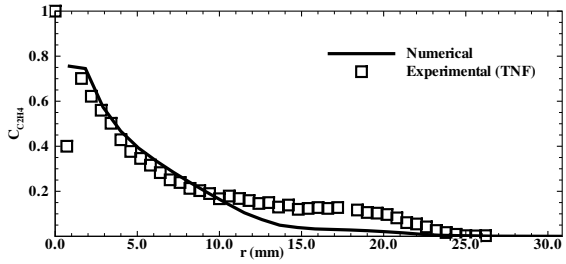

Figure 15. Comparison of predicted and measured radial profiles of the C_2H_4 mass fractions at $x/D_b = 1.0$ downstream from the base of the bluff body for non-reacting bluff-body burner with ethylene jet.

VI. Conclusions

A highly parallelized AMR scheme has been described for turbulent non-premixed combusting flows. The combination of a block-based AMR strategy and parallel implementation has resulted in a powerful computational tool, as demonstrated by the non-reacting and reacting flow results for the turbulent non-premixed flame bluff body burner. Future work will involve the extension of the algorithm to three-dimensional flow geometries and the application to more realistic combustor configurations.

VII. Acknowledgements

This research was supported by a Collaborative Research Opportunities Grant from the Natural Sciences and Engineering Research Council of Canada. Funding for the parallel computing facility used to perform the computations described herein was obtained from the Canadian Foundation for Innovation and Ontario Innovation Trust (CFI Project No. 2169). The authors are very grateful to these funding agencies for this support.

References

[1]Berger, M. J., "Adaptive Mesh Refinement for Hyperbolic Partial Differential Equations," *Journal of Computational Physics*, Vol. 53, 1984, pp. 484–512.

[2]Berger, M. J. and Colella, P., "Local Adaptive Mesh Refinement for Shock Hydrodynamics," *Journal of Computational Physics*, Vol. 82, 1989, pp. 67–84.

[3]Quirk, J. J., *An Adaptive Grid Algorithm for Computational Shock Hydrodynamics*, Ph.D. thesis, Cranfield Institute of Technology, January 1991.

[4]Powell, K. G., Roe, P. L., and Quirk, J., "Adaptive-Mesh Algorithms for Computational Fluid Dynamics," *Algorithmic Trends in Computational Fluid Dynmaics*, edited by M. Y. Hussaini, A. Kumar, and M. D. Salas, Springer-Verlag, New York, 1993, pp. 303–337.

[5]De Zeeuw, D. and Powell, K. G., "An Adaptively Refined Cartesian Mesh Solver for the Euler Equations," *Journal of Computational Physics*, Vol. 104, 1993, pp. 56–68.

[6]Quirk, J. J. and Hanebutte, U. R., "A Parallel Adaptive Mesh Refinement Algorithm," Report 93-63, ICASE, August 1993.

[7]Berger, M. J. and Saltzman, J. S., "AMR on the CM-2," *Applied Numerical Mathematics*, Vol. 14, 1994, pp. 239–253.

[8]Aftomis, M. J., Berger, M. J., and Melton, J. E., "Robust and Efficient Cartesian Mesh Generation for Component-Base Geometry," *AIAA Journal*, Vol. 36, No. 6, 1998, pp. 952–960.

[9]Groth, C. P. T., Zeeuw, D. L. D., Powell, K. G., Gombosi, T. I., and Stout, Q. F., "A Parallel Solution-Adaptive Scheme for Ideal Magnetohydrodynamics," Paper 99-3273, AIAA, June 1999.

[10]Groth, C. P. T., De Zeeuw, D. L., Gombosi, T. I., and Powell, K. G., "Global Three-Dimensional MHD Simulation of a Space Weather Event: CME Formation, Interplanetary Propagation, and and Interaction with the Magnetosphere," *Journal of Geophysical Research*, Vol. 105, No. A11, 2000, pp. 25,053–25,078.

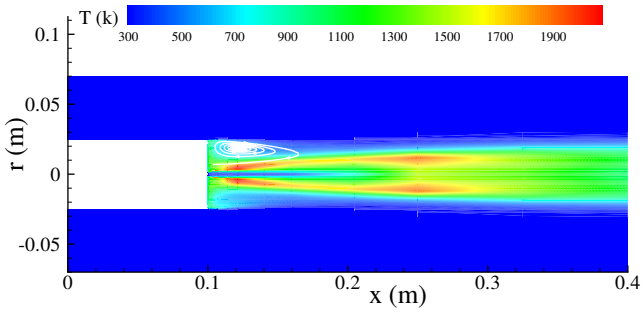

Figure 16. Predicted mean temperature distribution for combusting flow field of bluff-body burner.

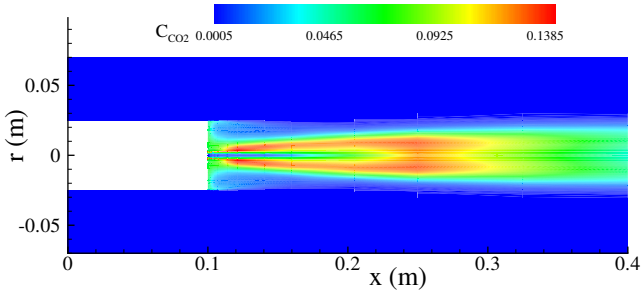

Figure 17. Predicted distribution of CO_2 mass fraction for combusting flow field of bluff-body burner.

[11]Sachdev, J. S., Groth, C. P. T., and Gottlieb, J. J., "A Parallel Solution-Adaptive Scheme for Predicting Multi-Phase Core Flows in Solid Propellant Rocket Motors," *International Journal of Computational Fluid Dynamics*, Vol. 19, No. 2, 2005, pp. 157–175.

[12]Bell, J., Day, M., Almgren, A., Lijewski, M. J., and Rendleman, C. A., "Adaptive Numerical Simulation of Turbulent Premixed Combustion," *Proceedings of the First MIT Conference on Computational Fluid and Solid Mechanics*, June 2001.

[13]Bell, J., Day, M., Almgren, A., Lijewski, M. J., and Rendleman, C. A., "A Parallel Adaptive Projection Method for Low Mach Number Flows," *International Journal for Numerical Methods in Fluids*, Vol. 40, 2002, pp. 209–216.

[14]Bell, J., "AMR for Low Mach Number Reacting Flow," http://repositories.cdlib.org/lbnl/ LBNL-54351, 2004.

[15]Douglas, C. C., Ern, A., and Smooke, M. D., "Numerical Simulation of Flames Using Multigrid Methods," *Iterative Methods in Scientific Computation*, edited by J. Wang, M. B. Allen, B. M. Chen, and T. Mathew, Vol. 4 of *IMACS Series in Computational and Applied Mathematics*, New Brunswick, 1998, pp. 149–154.

[16]Northrup, S. A. and Groth, C. P. T., "Solution of Laminar Diffusion Flames Using a Parallel Adaptive Mesh Refinement Algorithm," Paper 2005-0547, AIAA, January 2005.

[17]Wilcox, D. C., *Turbulence Modeling for CFD*, DCW Industries, La Cañada, 2002.

[18]Gordon, S. and McBride, B. J., "Computer Program for Calculation of Complex Chemical Equilibrium Compositions and Applications I. Analysis," Reference Publication 1311, NASA, 1994.

[19]McBride, B. J. and Gordon, S., "Computer Program for Calculation of Complex Chemical Equilibrium Compositions and Applications II. Users Manual and Program Description," Reference Publication 1311, NASA, 1996.

[20]Wilke, C. R., "A Viscosity Equation for Gas Mixtures," *Journal of Chemical Physics*, Vol. 18, 1950, pp. 517–519.

[21]Gardiner, W. C., *Combustion Chemistry*, Springer-Verlag New York Inc., Boca Raton, 1984.

[22]Westbrook, C. K. and Dryer, F. L., "Simplified Reaction Mechanisms for the Oxidation of Hydrocarbon Fuels in Flames," *Combustion Science and Technology*, Vol. 27, 1981, pp. 31–43.

[23]Poinsot, T. and Veynante, D., *Theoretical and Numerical Combustion*, R.T. Edwards Inc., 2001.

[24]Barth, T. J., "Recent Developments in High Order K-Exact Reconstruction on Unstructured Meshes," Paper 93-0668, AIAA, January 1993.

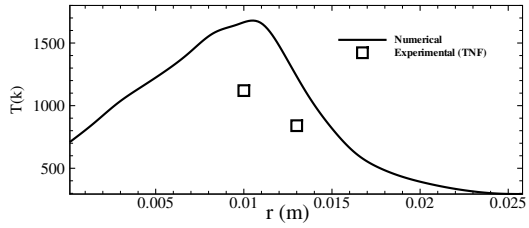

Figure 18. Predicted radial profile of mean temperature at $x/D_b = 1.92$ for combusting flow field of bluff-body burner.

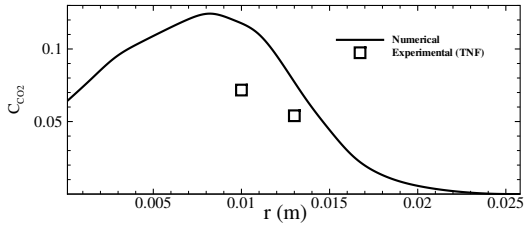

Figure 19. Predicted radial profile of CO_2 mass fraction at $x/D_b = 1.92$ for combusting flow field of bluff-body burner.

[25]Roe, P. L., "Approximate Riemann Solvers, Parameter Vectors, and Difference Schemes," *Journal of Computational Physics*, Vol. 43, 1981, pp. 357–372.

[26]Einfeldt, B., "On Godunov-Type Methods for Gas Dynamics," *SIAM Journal on Numerical Analysis*, Vol. 25, 1988, pp. 294–318.

[27]Linde, T., "A practical, general-purpose, two-state HLL Riemann solver for hyperbolic conservation laws," *International Journal for Numerical Methods in Fluids*, Vol. 40, 2002, pp. 391–402.

[28]Coirier, W. J. and Powell, K. G., "Solution-Adaptive Cartesian Cell Approach for Viscous and Inviscid Flows," *AIAA Journal*, Vol. 34, No. 5, May 1996, pp. 938–945.

[29]van Leer, B., Tai, C. H., and Powell, K. G., "Design of Optimally-Smoothing Multi-Stage Schemes for the Euler Equations," Paper 89-1933-CP, AIAA, June 1989.

[30]Liu, F. and Zheng, X., "A Strongly Coupled Time-Marching Method for Solving the Navier-Stokes and $k-\omega$ Turbulence Model Equations with Multigrid," *Journal of Computational Physics*, Vol. 128, No. 2, 1996, pp. 289–300.

[31]Park, S. H. and Kwon, J. H., "Implementation of $k-\omega$ Turbulence Models in An Implicit Multigrid Method," *AIAA Journal*, Vol. 42, No. 7, 2004, pp. 1348–1357.

[32]Gropp, W., Lusk, E., and Skjellum, A., *Using MPI*, MIT Press, Cambridge, Massachussets, 1999.

[33]Aftomis, M. J., Berger, M. J., and Murman, S. M., "Applications of Space-Filling Curves to Cartesian Methods for CFD," Paper 2004-1232, AIAA, January 2004.

[34]J.Laufer, "The Structure of Turbulence in Fully Developed Pipe Flow," Report 1174, NACA, 1954.

[35]"International Workshop on Measurement and Computation of Turbulent Nonpremixed Flames," http://www.ca.sandia.gov/TNF/.

[36]Dally, B. B., Fletcher, D. F., and Masri, A. R., "Flow and Mixing Fields of Turbulent Bluff-Body Jets and Flames," *Combustion Theory and Modelling*, Vol. 2, 1998, pp. 193–219.

[37]Turpin, G. and Troyes, J., "Validation of a Two-Equation Turbulence Model for Axisymmetric Reacting and Non-Reacting Flows," Paper 2000-3463, AIAA, July 2000.